Dynamical investigation and parameter stability region analysis of a flywheel energy storage system in charging mode*

Zhang Wei-Ya(张玮亚)†, Li Yong-Li(李永丽), Chang Xiao-Yong(常晓勇), and Wang Nan(王 楠)

Key Laboratory of Smart Grid of Ministry of Education, Tianjin University, Tianjin 300072, China
School of Electrical Engineering and Automation, Tianjin University, Tianjin 300072, China

(Received 20 February 2013; revised manuscript received 21 March 2013)

In this paper, the dynamic behavior analysis of the electromechanical coupling characteristics of a flywheel energy storage system (FESS) with a permanent magnet (PM) brushless direct-current (DC) motor (BLDCM) is studied. The Hopf bifurcation theory and nonlinear methods are used to investigate the generation process and mechanism of the coupled dynamic behavior for the average current controlled FESS in the charging mode. First, the universal nonlinear dynamic model of the FESS based on the BLDCM is derived. Then, for a 0.01 kWh/1.6 kW FESS platform in the Key Laboratory of the Smart Grid at Tianjin University, the phase trajectory of the FESS from a stable state towards chaos is presented using numerical and stroboscopic methods, and all dynamic behaviors of the system in this process are captured. The characteristics of the low-frequency oscillation and the mechanism of the Hopf bifurcation are investigated based on the Routh stability criterion and nonlinear dynamic theory. It is shown that the Hopf bifurcation is directly due to the loss of control over the inductor current, which is caused by the system control parameters exceeding certain ranges. This coupling nonlinear process of the FESS affects the stability of the motor running and the efficiency of energy transfer. In this paper, we investigate into the effects of control parameter change on the stability and the stability regions of these parameters based on the averaged-model approach. Furthermore, the effect of the quantization error in the digital control system is considered to modify the stability regions of the control parameters. Finally, these theoretical results are verified through platform experiments.

Keywords: flywheel energy storage system, Hopf bifurcation mechanism, Routh stability criterion, parameter stability regions

PACS: 84.50.+d, 84.60.Ve, 05.45.–a **DOI:** 10.1088/1674-1056/22/9/098401

1. Introduction

The permanent magnet (PM) brushless direct-current (DC) motor (BLDCM) controlled flywheel energy storage system (FESS) is becoming a new type of energy storage system due to its simplicity in storing kinetic energy. The FESS is used to take electric energy from a power network when in the charging mode, store it in the form of rotating kinetic energy, and deliver it according to the load's need in the discharging mode. The energy conversion is accomplished by power electronic circuits. With several advantages such as high efficiency in a wide operating range, low maintenance, greater durability, compactness, and higher power density, the FESS has become a primary technology used to compensate for power interruptions, smoothing of delivered power, and providing short power interruption protection.

The FESS, including a BLDC motor, power electronic circuits, and feedback controllers, is a multi-variable, nonlinear, and strongly electromechanical coupling system. Though they have not been perceived or observed, the irregular movements of the FESS occur all the time.[1–3] The chaotic behavior brings up complex issues both inside and outside the FESS. This irregular phenomenon gives rise to torque instability and electrical oscillation in the FESS itself;[4] at the same time, it causes harmonic pollution and frequency instability in the system connected to the FESS. In recent years, the rotor dynamics of the FESS has been widely studied. Coombs *et al.*[5] studied the rotor dynamics of the flywheel system with the control system factors considered, the dynamics differential equations were established, and the coupling relationship between dynamic response and torque was obtained by real time simulation. In Ref. [4], the electromechanical nonlinear dynamic model of the FESS with a hybrid permanent magnetic-dynamic spiral groove bearing was first established. Chen[6] established the dynamics model of an electric vehicle flywheel with rolling bearings by using the finite-element method. In Ref. [7], a nonlinear dynamic model of the permanent magnet motor based mechanical elastic energy storage (MEES) unit was derived, and the chaotic behavior under certain parameters and operation conditions was demonstrated. Existing investigations mostly focus on the chaotic phenomena of the rotor dynamics of the flywheel, but the coupled dynamic behavior of the FESS, especially the dynamic interaction between the power electronic subsystem and the mechanical subsystem has been neither systematically studied nor thoroughly under-

*Project supported by the National Basic Research Program of China (Grant No. 2009CB2197), the National Natural Science Foundation of China (Grant No. 51177108), and the Specialized Research Fund for the Doctoral Program of Higher Education of China (Grant No. 20110032110066).

†Corresponding author. E-mail: zhangweiyatju@126.com

© 2013 Chinese Physical Society and IOP Publishing Ltd

stood. The electromechanical coupling dynamic behavior not only leads to the self-excited vibration of the energy transferring process, but also results in the global instability of the FESS.

In this paper, based on the previous research, we discuss a nonlinear dynamic model and the generation mechanism of nonlinear dynamic behavior in a current-mode controlled FESS working in the charging mode.[8–11] The quantitative analysis of the nonlinear dynamic behavior and the physical mechanism of bifurcation in such a system are also discussed. For this purpose, the numerical time domain simulation and averaged model approach are combined in the analysis. According to the bifurcation diagrams and the nonlinear dynamical theory, the characteristics of the Hopf bifurcation, the variation rule of the oscillation period, as well as the mechanism for the low-frequency oscillation in the electromechanical coupling system are investigated systematically. The approach adopted in this paper is clear logically and well-defined physically, which makes it useful in forecasting and discovering the chaotic behavior in the FESS or other similar systems.

2. Electromechanical coupling model and bifurcation characteristics of FESS

2.1. Electromechanical coupling model

The topology of the FESS is plotted in Fig. 1. It mainly contains a power electronic subsystem (including a bi-directional buck-boost converter and a three-phase full bridge converter), a mechanical subsystem (BLDCM with a flywheel), and a feedback control subsystem. In order to absorb the transient increase of power as quickly as possible, the control system of the FESS in the charging mode is designed to have a two-stage strategy, which includes an average current control and a maximum speed limit control. When a power increase is detected, the FESS will store energy immediately to limit the current within boundaries according to the average current control strategy. Thus the security of the whole system is ensured by this operation. If the speed limit of the BLDCM is taken into account, the maximum speed limit control program will be executed when necessary. By counting the Hall signals which are generated by the Hall sensing component cycle by cycle, the control system outputs a speed signal used to determine whether the speed of the BLDCM is out of limit, and the charging mode will be shut down when necessary. This paper only focuses on the normal charging mode controlled by the average current control method, and the maximum speed limit control is not included in the discussion.

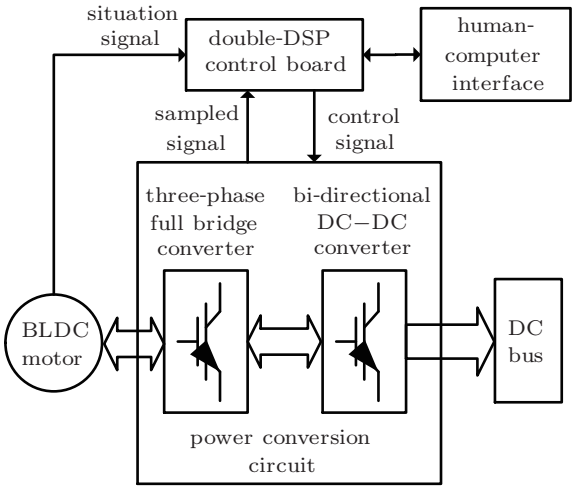


Fig. 1. Flywheel energy storage system.

The schematic diagram of an average current control FESS in the charging mode is shown in Fig. 2. The feedback control subsystem generates a pulse width modulation (PWM) signal to drive the switch V1 of the bi-directional buck-boost converter. Thus, the converter can supply the BLDCM with electrical energy to achieve the average current control by adjusting the duty cycle of switch V1. The VT1, VT2, …, VT6 in the three-phase full bridge converter can be controlled by the control system, which utilizes the Hall signal in the BLDCM, thereby ensuring that the phase reversing operation of the BLDCM operates correctly.

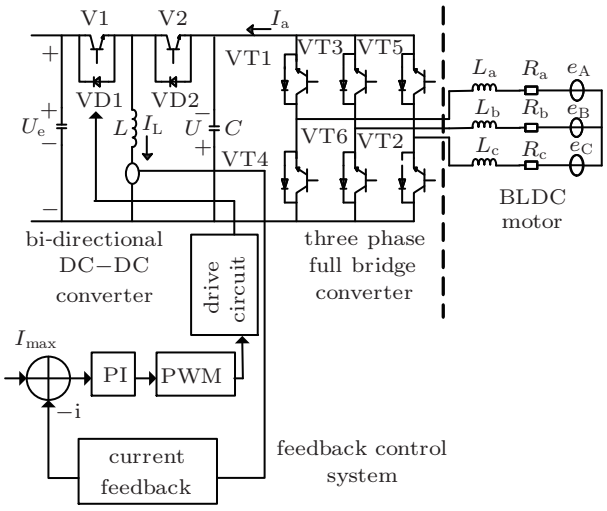


Fig. 2. Schematic diagram of a charging mode closed-loop current-programmed FESS.

If the circuit operates in the continuous mode, namely, the inductor current $i_L > 0$ in a switching cycle, the circuit has two modes when switch V and diode VD are turned on or off, i.e., mode 1 ($nT < t < nT + \mathrm{d}T$) in which switch V1 turns on and diode VD2 turns off; mode 2 ($nT + \mathrm{d}T < t < (n+1)T$) in which switch V1 turns off and diode VD2 turns on. To derive the state equations in each switch state, the corresponding

equivalent circuit of the FESS is given in Fig. 3. The exact state equations corresponding to each switch state can be written as follows:

$$\begin{aligned}
&\text{mode 1}\ \ (nT < t < nT + \mathrm{d}T):\\
&\begin{cases}
\dfrac{\mathrm{d}i_L}{\mathrm{d}t} = \dfrac{U_\mathrm{e}}{L},\\
\dfrac{\mathrm{d}v}{\mathrm{d}t} = -\dfrac{i_\mathrm{a}}{C},\\
\dfrac{\mathrm{d}i_\mathrm{a}}{\mathrm{d}t} = \dfrac{v}{L_\mathrm{m}} - \dfrac{K_\mathrm{e}\omega}{L_\mathrm{m}} - \dfrac{R_\mathrm{m}i_\mathrm{a}}{L_\mathrm{m}},\\
\dfrac{\mathrm{d}\omega}{\mathrm{d}t} = \dfrac{K_\mathrm{m}i_\mathrm{a}}{J} - \dfrac{B_\mathrm{v}\omega}{J} - \dfrac{T_\mathrm{L}}{J},
\end{cases}\\
&\text{mode 2}\ \ (nT + \mathrm{d}T < t < (n+1)T):\\
&\begin{cases}
\dfrac{\mathrm{d}i_L}{\mathrm{d}t} = -\dfrac{v}{L},\\
\dfrac{\mathrm{d}v}{\mathrm{d}t} = \dfrac{i_L}{C} - \dfrac{i_\mathrm{a}}{C},\\
\dfrac{\mathrm{d}i_\mathrm{a}}{\mathrm{d}t} = \dfrac{v}{L_\mathrm{m}} - \dfrac{K_\mathrm{e}\omega}{L_\mathrm{m}} - \dfrac{R_\mathrm{m}i_\mathrm{a}}{L_\mathrm{m}},\\
\dfrac{\mathrm{d}\omega}{\mathrm{d}t} = \dfrac{K_\mathrm{m}i_\mathrm{a}}{J} - \dfrac{B_\mathrm{v}\omega}{J} - \dfrac{T_\mathrm{L}}{J},
\end{cases}
\end{aligned} \tag{1}$$

where i_L is the current in the inductor L of the bi-directional buck-boost converter, v is the voltage of the capacity C, i_a is the current in the equivalent BLDCM, ω is the angular velocity of the BLDCM, U_e is the DC bus voltage, K_e is the back-EMF constant, K_m is the torque constant, B_v is the equivalent viscous damping, J is the load inertia, R_m is the resistance of motor's winding, L_m is the equivalent inductance of the motor's winding, and T_L is the load torque.

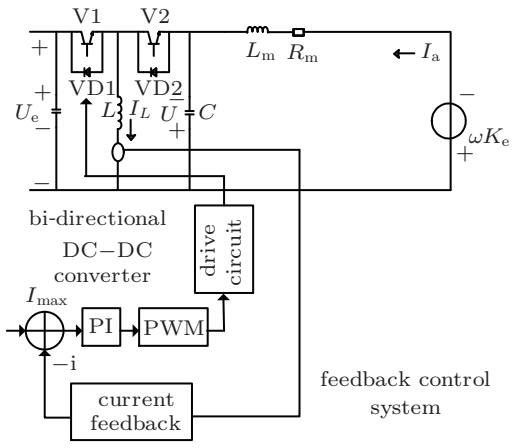


Fig. 3. Equivalent circuit of FESS shown in Fig. 2.

The compensation effect plays an important part in the control loop because it can gain robustness for the whole system: an integral control should be included in the control loop to satisfy the no-limit-cycle condition. Thus, the proportional-integral (PI) control is used to compensate for the average current error. The proportional coefficient is K_pi, the integral coefficient is K_ii, and the sampling coefficients of voltage and current are h_v and h_i, respectively. The output of the compensator $y_\mathrm{c}(t)$ can be described in the continuous time domain by

$$\begin{cases}
\dot{X}_\mathrm{c}(t) = -h_\mathrm{i}i_L(t) + h_\mathrm{i}I_\mathrm{ref},\\
y_\mathrm{c}(t) = K_\mathrm{pi}h_i(I_\mathrm{ref} - i_L(t)) + K_\mathrm{ii}X_\mathrm{c}(t),
\end{cases} \tag{2}$$

where $X_\mathrm{c}(t) = [x_{1\mathrm{c}}(t)]$ is the control state vector, $I_\mathrm{ref} = I_\mathrm{max}$ is the reference value of the PI. Assume that U_saw is the independent sawtooth ramp voltage of the control system, when $y_\mathrm{c}(t) > U_\mathrm{saw}$, the system operates in mode 1, when $y_\mathrm{c}(t) < U_\mathrm{saw}$, the system operates in mode 2.

With the above analysis, the exact state equations corresponding to each switch state can be derived as follows:

$$\begin{cases}
\dot{\boldsymbol{X}}(t) = \boldsymbol{A}_1\boldsymbol{X}(t) + \boldsymbol{B}_1\boldsymbol{U} + \boldsymbol{B}_{1\mathrm{r}}\boldsymbol{I}_\mathrm{ref}, & \text{mode 1},\\
\dot{\boldsymbol{X}}(t) = \boldsymbol{A}_2\boldsymbol{X}(t) + \boldsymbol{B}_2\boldsymbol{U} + \boldsymbol{B}_{2\mathrm{r}}\boldsymbol{I}_\mathrm{ref}, & \text{mode 2},
\end{cases} \tag{3}$$

where

$$\boldsymbol{A}_1 = \begin{bmatrix}
0 & 0 & 0 & 0 & 0\\
0 & 0 & -\dfrac{1}{C} & 0 & 0\\
0 & \dfrac{1}{L_\mathrm{m}} & -\dfrac{R_\mathrm{m}}{L_\mathrm{m}} & -\dfrac{K_\mathrm{e}}{L_\mathrm{m}} & 0\\
0 & 0 & \dfrac{K_\mathrm{m}}{J} & -\dfrac{B_\mathrm{v}}{J} & 0\\
-h_\mathrm{i} & 0 & 0 & 0 & 0
\end{bmatrix},$$

$$\boldsymbol{A}_2 = \begin{bmatrix}
0 & -\dfrac{1}{L} & 0 & 0 & 0\\
\dfrac{1}{C} & 0 & -\dfrac{1}{C} & 0 & 0\\
0 & \dfrac{1}{L_\mathrm{m}} & -\dfrac{R_\mathrm{m}}{L_\mathrm{m}} & -\dfrac{K_\mathrm{e}}{L_\mathrm{m}} & 0\\
0 & 0 & \dfrac{K_\mathrm{m}}{J} & -\dfrac{B_\mathrm{v}}{J} & 0\\
-h_\mathrm{i} & 0 & 0 & 0 & 0
\end{bmatrix},$$

$$\boldsymbol{B}_1 = \begin{bmatrix} \dfrac{1}{L} & 0 & 0 & -\dfrac{1}{J} & 0 \end{bmatrix}^\mathrm{T}, \quad \boldsymbol{B}_2 = \begin{bmatrix} 0 & 0 & 0 & -\dfrac{1}{J} & 0 \end{bmatrix}^\mathrm{T},$$

$$\boldsymbol{B}_{1\mathrm{r}} = \begin{bmatrix} 0 & 0 & 0 & 0 & h_\mathrm{i} \end{bmatrix}^\mathrm{T}, \quad \boldsymbol{B}_{2\mathrm{r}} = \begin{bmatrix} 0 & 0 & 0 & 0 & h_\mathrm{i} \end{bmatrix}^\mathrm{T},$$

$$\boldsymbol{U} = \begin{bmatrix} U_\mathrm{e} & 0 & 0 & T_\mathrm{L} & 0 \end{bmatrix}^\mathrm{T},$$

$$\boldsymbol{X}(t) = [\, i_L(t)\ \ v(t)\ \ i_\mathrm{a}(t)\ \ \omega(t)\ \ x_{1\mathrm{c}}(t)\,]^\mathrm{T}.$$

2.2. Bifurcation characteristics

From Eq. (3), it can be seen that the topology of the circuits varies according to the state of the switch and the inductor current in the bi-directional buck-boost converter. Two consecutive dynamic behaviors are involved in the charging mode, each of the dynamic behaviors is linear yet the overall dynamic behavior is nonlinear, which is referred to as piecewise nonlinearity. Besides, the multiplication operation in the BLDCM makes the behavior of the FESS more complex. The dynamic behavior of the power electronic subsystem can influence the electrical characteristics in the mechanical subsystem. The reverse influence of the mechanical subsystem on the power electronic subsystem exists as well.

Simulation models have been built according to the set of parameters in Table 1, which originate from the previously developed FESS platform. A series of computer simulations is carried out to make an initial evaluation of the possible bifurcation phenomena. In order to observe the effect of the feedback control subsystem on the dynamic behavior of the FESS, we restrict our attention to the case where K_{pi} and K_{ii} are the control variables and the other parameters are treated as fixed parameters. Figures 4 and 5 show the current waveforms of i_L, the output voltage waveforms of v, and angular velocity ω for the BLDCM with various K_{ii} at $K_{pi} = 6$. Figure 4 shows that at $K_{ii} = 1$, the inductor current i_L follows the input current reference, and the output voltage v and ω are approximately constant. As K_{ii} increases, when $K_{ii} = 9.5$, the normal operation is no longer possible, and the system begins to exhibit a limit cycle oscillation, where the Hopf bifurcation occurs and a quasi-periodic orbit takes place, consequently the oscillation amplitude increases to a comparatively large value. Obviously, the amplitude and the frequency of the oscillation both become steady and time-independent on the time scale slower than the switching frequency. The inherent behavior of the system is shown as a self-period oscillation, instead of a non-recurring, randomly generated phenomenon. From the nonlinear viewpoint, the occurrence of the low-frequency quasi-periodic orbit reflects that the system undergoes a Hopf bifurcation.[12,13] From a physical point of view, the system behavior is characterized by the existence of two different incommensurate frequencies. One is the switching frequency, while the other is related to the system parameters, which can be derived by computing the characteristic multipliers of the system when the Hopf bifurcation occurs.

Meanwhile, when the Hopf bifurcation occurs, the phase current in the BLDCM is shown in Fig. 5(e), from which a periodic oscillation together with the slow-scale instability of the power electronics subsystem can be seen. The input power P of the BLDCM is shown in Fig. 5(f), the periodically varying power affects the stability of the torque of the BLDCM, reduces the efficiency of the FESS, and has a bad influence on the stability of the whole FESS. Finally, in order to better illustrate the dynamic behavior, some FFT spectra are measured. Figures 5(g)–5(h) illustrate the FFT spectra of i_L and P under the Hopf bifurcation, in which the waveforms of i_L and P contain not only the fundamental wave component but also the harmonic components (about 266 Hz).

Table 1. Parameters of FESS.

Parameter	Value
DC bus voltage U_e	48 V
Transfer inductance L	0.0007 H
Filter capacitor C	0.001 F
Resistance of the motor's winding R_m	0.5 Ω
Inductance of the motor's winding L_m	0.0036 H
Torque constant K_m	7 V/krpm
Back-EMF constant K_e	6.5 V/krpm
Viscous damping B_v	0.0001 N·m/rad/s
Load inertia J	0.123 N·m/rad/s^2
Load torque T_L	0.1 N·m

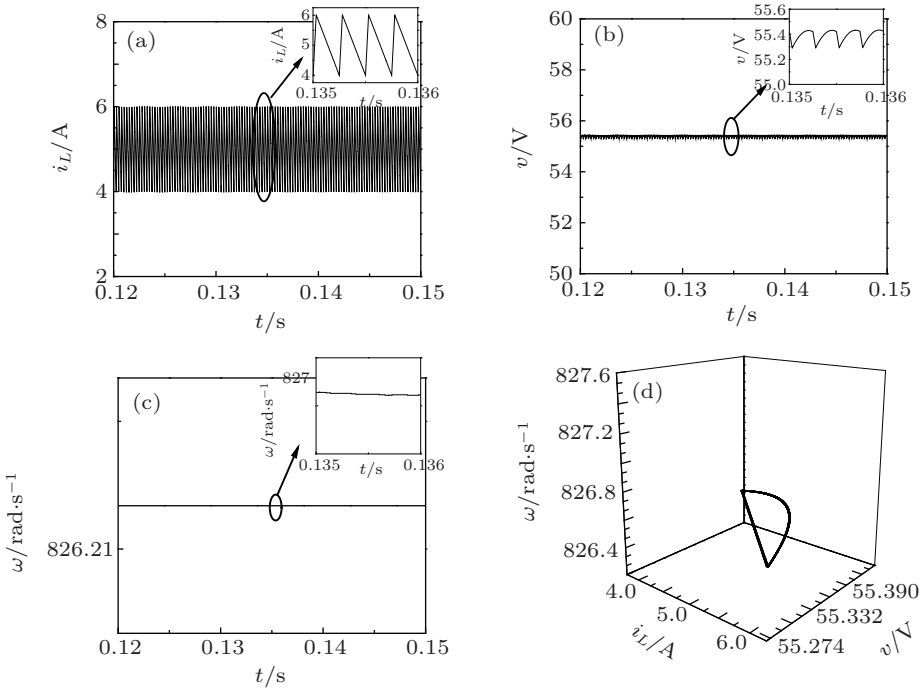


Fig. 4. Evolution of system states under $K_{pi} = 6$ and $K_{ii} = 1$: (a) waveforms of i_L, (b) waveforms of v, (c) waveforms of ω, (d) three-dimensional trajectory of i_L, v, and ω.

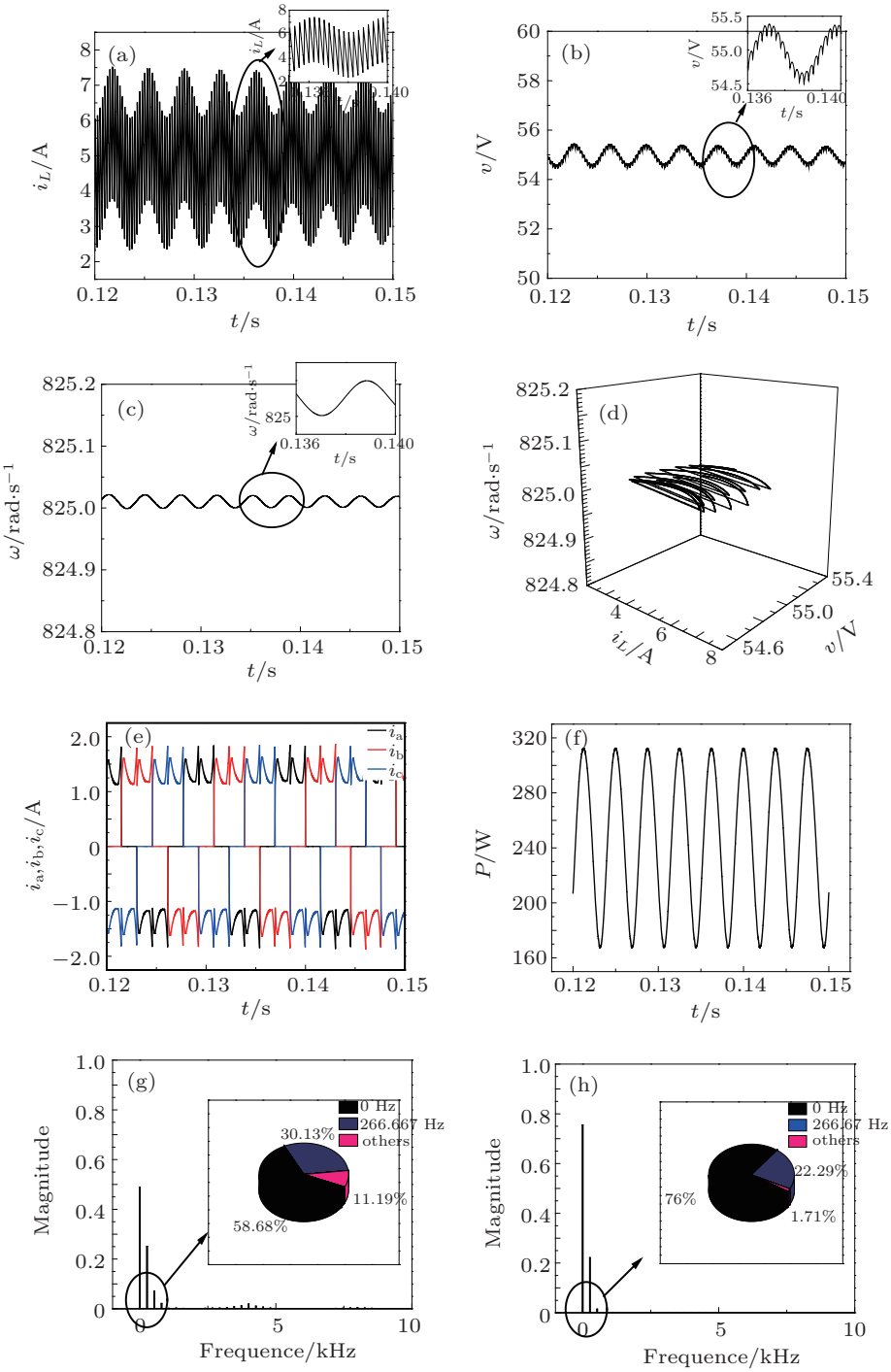


Fig. 5. (color online) Evolution of system states under $K_{\rm pi} = 6$ and $K_{\rm ii} = 9.5$: (a) waveforms of i_L, (b) waveforms of v, (c) waveforms of ω, (d) three-dimensional trajectory of i_L, v, and ω, (e) the phase current in the BLDCM, (f) input power of the BLDCM, (g) FFT spectra analysis of i_L, (h) FFT spectra analysis of P.

3. Evolution analysis and mechanism study of the Hopf bifurcation

3.1. Evolution analysis for the Hopf bifurcation

In order to check the dynamic performance of the FESS, assume $x_n = x_{nT} = X(nT)$ to be the instantaneous electrical value at time instant $t = nT$ when the switch is turned off, and $x_{n+1} = x_{(n+1)T} = X((n+1)T)$ to be the instantaneous electrical value at time instant $t = (n+1)T$ when the switch begins a new cycle, as shown in Fig. 6. By using a successive substitution method, the value of x_{n+1} can be calculated through Eq. (4) as

$$\begin{aligned} x_{n+1} &= f(x_n, d_n) \\ &= N_{\rm off}(1-d_n)N_{\rm on}(d_n)x_n + N_{\rm off}(1-d_n)M_{\rm on}(d_n) \\ &\quad \times (\boldsymbol{B}_1 U + \boldsymbol{B}_{1\rm r} I_{\rm ref}) + M_{\rm off}(1-d_n)(\boldsymbol{B}_2 U + \boldsymbol{B}_{2\rm r} I_{\rm ref}), \end{aligned} \tag{4}$$

where

$$N_{\rm on}(d_n) = {\rm e}^{\boldsymbol{A}_1 d_n T}, \quad N_{\rm off}(1-d_n) = {\rm e}^{\boldsymbol{A}_2(1-d_n)T},$$
$$M_{\rm on}(d_n) = \int_0^{d_n T} {\rm e}^{\boldsymbol{A}_1(d_n T-\tau)}\,{\rm d}\tau,$$
$$M_{\rm off}(1-d_n) = \int_{d_n T}^{T} {\rm e}^{\boldsymbol{A}_2(T-\tau)}\,{\rm d}\tau.$$

Assume that $U_{\rm ramp}$ is the independent sawtooth peak voltage of the control system, define the switching function as

$$s(d_n, x_n) = \boldsymbol{C}_s x_n + K_{\rm pi} h_{\rm i} I_{\rm ref} - d_n U_{\rm ramp} = 0, \tag{5}$$

where $\boldsymbol{C}_s = [\,-K_{\rm pi}h_{\rm i}\ 0\ 0\ 0\ K_{\rm ii}\,]$.

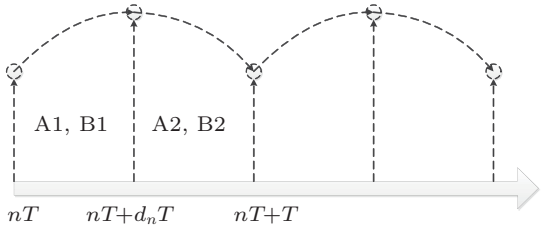


Fig. 6. Schematic diagram of the state switching.

Due to Eqs. (4) and (5), the continuous-time dynamical system can be modeled by an iterative map, also known as the stroboscopic map. Although the analytical derivation of this stroboscopic map is not discussed in this paper, the phase portraits of such a stroboscopic map will be used to identify the qualitative nature of the observed dynamical behavior. Moreover, the bifurcation diagram is also plotted with the data generated from the stroboscopic map.

3.1.1. Influence of the power electronic subsystem on the mechanical subsystem's dynamics

In the switching mode, the dynamic behavior in the power electronic subsystem disturbs the input energy of the mechanical subsystem all the time. First, set $K_{\rm pi} = 6$, increase $K_{\rm ii}$ gradually, and then collect the steady state of the sampled data at the switching frequency at the turn-off instants. With the sufficient number of sampled data, the bifurcation diagrams can be constructed as required. The bifurcation diagram of $K_{\rm ii}$ is depicted in Fig. 7(a), from which it can be clearly seen that at first the inductor current i_L settles at the period-1 steady state and then at about $K_{\rm ii} = 7.3$, the slow-scale oscillation shows up. The sampled inductor current amplitude keeps increasing and shows large variations subsequently, which degrades the system performance significantly. The Poincaré section tool is constructed and used to verify the existence of different behaviors in Fig. 7(a), including the period-1 steady state and the Hopf bifurcation state in Figs. 7(b) and 7(c). When the Hopf bifurcation appears, the power electronic subsystem influences the input voltage of the mechanical subsystem and leads to torque instability.

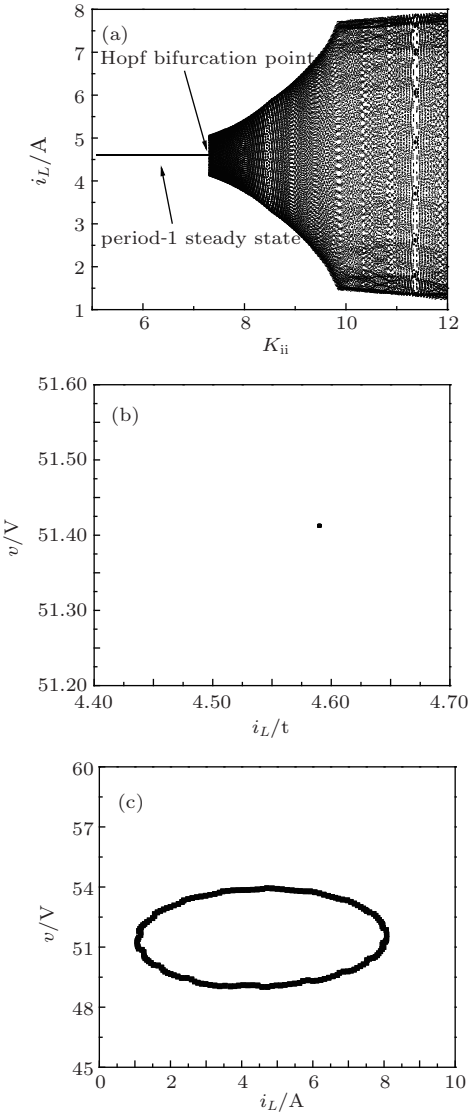


Fig. 7. (a) Bifurcation diagram with $K_{\rm ii}$ as the bifurcation parameter, (b) Poincaré section of period-1 steady state in panel (a), (c) Poincaré section of Hopf bifurcation state in panel (a).

3.1.2. Influence of the mechanical subsystem on the power electronic subsystem's dynamics

As a load of the power electronic subsystem, the variations in the design parameters of the BLDCM including the mechanical and electromagnetic parameters such as stiffness and damping coefficient of both the upper and the lower dampers can deeply influence the behaviors of the motor body, and deliver the disturbance back to the former stage as well. Set $K_{\rm pi} = 6$ and $K_{\rm ii} = 1$, increase $L_{\rm m}$ gradually, and then collect the steady state of the sampled data in the same way, the bifurcation diagram of i_L is obtained and depicted in Fig. 8(a), from which it can be clearly seen that at first the inductor current i_L settles at the period-1 steady state and then at about $L_{\rm m} = 3.9$ mH, the Hopf bifurcation shows up, which verifies that the reverse influence of the mechanical subsystem on the power electronic subsystem exists as well.

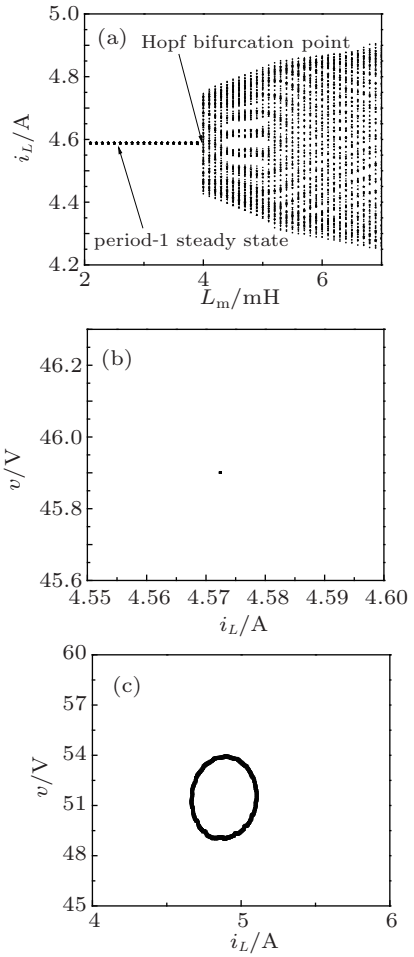


Fig. 8. (a) Bifurcation diagram with L_m serving as the bifurcation parameter, (b) Poincaré section of period-1 steady state in panel (a), (c) Poincaré section of Hopf bifurcation state in panel (a).

3.2. Mechanism study of the Hopf bifurcation

3.2.1. Jacobian matrix and Routh stability criterion

The averaged model approach is a commonly adopted method to understand the operating physical meaning of converters, in which the switching details are neglected and only the envelope of the dynamical motion is taken into account.[14,15] During the operation of the charging mode of the FESS, the duty ratio d meets the requirement $D_{\min} \le d \le D_{\max}$. By setting all the derivatives to be zero, the following equations can be obtained:

$$\begin{cases} \dfrac{\mathrm{d}\langle i_L(t)\rangle}{\mathrm{d}t} = \dfrac{d-1}{L}\langle v(t)\rangle + \dfrac{\mathrm{d}U_e}{L} = 0, \\ \dfrac{\mathrm{d}\langle v(t)\rangle}{\mathrm{d}t} = \dfrac{1-d}{C}\langle i_L(t)\rangle - \dfrac{1}{C}\langle i_a(t)\rangle = 0, \\ \dfrac{\mathrm{d}\langle i_a(t)\rangle}{\mathrm{d}t} = \dfrac{1}{L_m}\langle v(t)\rangle - \dfrac{R_m}{L_m}\langle i_a(t)\rangle - \dfrac{K_e}{L_m}\langle \omega(t)\rangle = 0, \\ \dfrac{\mathrm{d}\langle \omega(t)\rangle}{\mathrm{d}t} = \dfrac{K_m}{J}\langle i_a(t)\rangle - \dfrac{B_v}{J}\langle \omega(t)\rangle - \dfrac{T_L}{J} = 0, \\ \dfrac{\mathrm{d}\langle x_{1c}(t)\rangle}{\mathrm{d}t} = -h_i\langle i_L(t)\rangle + h_i I_{ref} = 0, \end{cases} \tag{6}$$

where $\langle i_L(t)\rangle$, $\langle v(t)\rangle$, $\langle i_a(t)\rangle$, $\langle \omega(t)\rangle$, and $\langle x_{1c}(t)\rangle$ are the average values of i_L, v, i_a, ω, and x_{1c} during a switching cycle, and d is the duty ratio and can be expressed as

$$d = [K_{ii}\langle x_{1c}(t)\rangle + K_{pi}h_i I_{ref} - K_{pi}h_i\langle i_L(t)\rangle]/U_{ramp}. \tag{7}$$

Combining Eq. (6) with Eq. (7), we can derive the fixed point as

$$\begin{bmatrix} I_L & V & I_a & O & X_{1c} \end{bmatrix}^{\mathrm{T}} = \begin{bmatrix} I_{ref} & \dfrac{DU_e}{1-D} & (1-D)I_{ref} & \dfrac{K_m(1-D)I_{ref} - T_L}{B_v} & \dfrac{DU_{ramp}}{K_{ii}} \end{bmatrix}^{\mathrm{T}}. \tag{8}$$

Equations (6)–(8) can be combined to obtain the stable duty ratio

$$D = \frac{\sqrt{(2a-b+1)^2 - 4a(a-b)} + 2a - b + 1}{2a}, \tag{9}$$

where

$$a = \frac{(K_eK_m + B_vR_m)I_{ref}}{B_vU_e}, \quad b = \frac{K_eT_L}{B_vU_e}.$$

Combined with the average model discussed above, the Jacobian matrix of the fixed point is

$$\boldsymbol{J}(x) = \begin{bmatrix} -\dfrac{K_{pi}h_i(U_e+V)}{LU_{ramp}} & \dfrac{-K_{pi}h_iI_L + K_{ii}X_{1c} + K_{pi}h_iI_{ref} - U_{ramp}}{LU_{ramp}} & 0 & 0 & \dfrac{K_{ii}(U_e+V)}{LU_{ramp}} \\ \dfrac{U_{ramp} - K_{pi}h_iI_{ref} + 2K_{pi}h_iI_L - K_{ii}X_{1c}}{CU_{ramp}} & 0 & -\dfrac{1}{C} & 0 & -\dfrac{K_{ii}I_L}{CU_{ramp}} \\ 0 & \dfrac{1}{L_m} & -\dfrac{R_m}{L_m} & -\dfrac{K_e}{L_m} & 0 \\ 0 & 0 & \dfrac{K_m}{J} & -\dfrac{B_v}{J} & 0 \\ -h_i & 0 & 0 & 0 & 0 \end{bmatrix}. \tag{10}$$

The characteristic equation of matrix $\boldsymbol{J}(x)$ is

$$\det[\lambda \boldsymbol{I} - \boldsymbol{J}(x)] = 0. \tag{11}$$

From Eq. (11), we have the characteristic equation of the closed-loop transfer function

$$a_0\lambda^5 + a_1\lambda^4 + a_2\lambda^3 + a_3\lambda^2 + a_4\lambda + a_5 = 0. \tag{12}$$

Set

$$s_1 = \frac{K_{\mathrm{pi}}h_{\mathrm{i}}(U_{\mathrm{e}}+V)}{LU_{\mathrm{ramp}}},$$
$$s_2 = \frac{-K_{\mathrm{pi}}h_{\mathrm{i}}I_L + K_{\mathrm{ii}}X_{1\mathrm{c}} + K_{\mathrm{pi}}h_{\mathrm{i}}I_{\mathrm{ref}} - U_{\mathrm{ramp}}}{LU_{\mathrm{ramp}}},$$
$$s_3 = \frac{K_{\mathrm{ii}}(U_{\mathrm{e}}+V)}{LU_{\mathrm{ramp}}},$$
$$s_4 = \frac{U_{\mathrm{ramp}} - K_{\mathrm{pi}}h_{\mathrm{i}}I_{\mathrm{ref}} + 2K_{\mathrm{pi}}h_{\mathrm{i}}I_L - K_{\mathrm{ii}}X_{1\mathrm{c}}}{CU_{\mathrm{ramp}}},$$
$$s_5 = -\frac{K_{\mathrm{ii}}I_L}{CU_{\mathrm{ramp}}},$$

then we have

$$a_0 = 1,$$
$$a_1 = \frac{B_{\mathrm{v}}CL_{\mathrm{m}} + CJR_{\mathrm{m}} + CJL_{\mathrm{m}}s_1}{CJL_{\mathrm{m}}},$$
$$a_2 = \frac{J + B_{\mathrm{v}}CR_{\mathrm{m}} + CK_{\mathrm{e}}K_{\mathrm{m}} + B_{\mathrm{v}}CL_{\mathrm{m}}s_1 + CJR_{\mathrm{m}}s_1 + CJL_{\mathrm{m}}h_{\mathrm{i}}s_3 - CJL_{\mathrm{m}}s_2s_4}{CJL_{\mathrm{m}}},$$
$$a_3 = -\frac{Js_1 - B_{\mathrm{v}} - B_{\mathrm{v}}CR_{\mathrm{m}}s_1 - CK_{\mathrm{e}}K_{\mathrm{m}}s_1 - CB_{\mathrm{v}}L_{\mathrm{m}}h_{\mathrm{i}}s_3 + B_{\mathrm{v}}CL_{\mathrm{m}}s_2s_4 - CJh_{\mathrm{i}}R_{\mathrm{m}}s_3 + CJR_{\mathrm{m}}s_2s_4 - CJL_{\mathrm{m}}h_{\mathrm{i}}s_2s_5}{CJL_{\mathrm{m}}},$$
$$a_4 = \frac{Jh_{\mathrm{i}}s_3 + B_{\mathrm{v}}s_1 + B_{\mathrm{v}}Ch_{\mathrm{i}}R_{\mathrm{m}}s_3 + CK_{\mathrm{e}}h_{\mathrm{i}}K_{\mathrm{m}}s_3 - B_{\mathrm{v}}CR_{\mathrm{m}}s_2s_4 - CK_{\mathrm{e}}K_{\mathrm{m}}s_2s_4 + B_{\mathrm{v}}CL_{\mathrm{m}}h_{\mathrm{i}}s_2s_5 + CJR_{\mathrm{m}}h_{\mathrm{i}}s_2s_5}{CJL_{\mathrm{m}}},$$
$$a_5 = \frac{B_{\mathrm{v}}h_{\mathrm{i}}s_3 + B_{\mathrm{v}}CR_{\mathrm{m}}h_{\mathrm{i}}s_2s_5 + CK_{\mathrm{e}}K_{\mathrm{m}}h_{\mathrm{i}}s_2s_5}{CJL_{\mathrm{m}}}. \tag{13}$$

According to the Routh stability criterion, if all elements of the first column of the Routh array (see Table 2) are nonzero and have the same sign, the system is stable.[14,16] Hence, considering the boundary condition $T_1 > 0$, $T_2 > 0$, $T_3 > 0$, $T_4 > 0$, $T_5 > 0$, and $T_6 > 0$, the stable equation can be obtained as

$$0 < K_{\mathrm{ii}} < \delta(I_{\max}, K_{\mathrm{pi}}). \tag{14}$$

Table 2. Routh table.

λ^5	$T_1 = a_0$	a_2	a_4
λ^4	$T_2 = a_1$	a_3	a_5
λ^3	$T_3 = \frac{a_1a_2 - a_0a_3}{a_1}$	$T_{31} = \frac{a_1a_4 - a_0a_5}{a_1}$	0
λ^2	$T_4 = \frac{T_3a_3 - a_1a_4 + a_0a_5}{T_3}$	$T_{41} = a_5$	0
λ^1	$T_5 = \frac{a_1a_4 - a_0a_5}{a_1} - \frac{a_5}{T_4}$	0	0
λ^0	$T_6 = a_5$	0	0

3.2.2. Physical mechanism of the Hopf bifurcation

From the perspective of energy, the power and control circuits of the FESS together constitute a phase-shifting and frequency-selecting unit. When the system is in the continuous conduction mode (CCM), the state variables have the trend to expand; while in the discontinuous conduction mode (DCM), the state variables have the trend to shrink to the fixed points. Thus the whole system presents enlarged nonlinear characteristics as switching between CCM and DCM. With the operation mode changing back and forth, the frequency and amplitude of the slow oscillation can be limited to a certain range. As a strongly nonlinear system, the FESS contains both expansion and contraction factors. On the other hand, as an energy conversion device, the FESS should have the ability to release and consume energy. The energy release can be seen as the expansion factor, while the energy consumption can be regarded as the contraction factor. Furthermore, enhancing the energy expansion harms the stability of the system while increasing the energy consumption increases the stability of the system.

The energy release and augmented consumption verifying the generalized existence of bifurcation is reasonable, and the perspective of the physical mechanism will help explain the route to chaos in depth. Further mechanism analysis can be proposed according to the nonlinear system theory by examining the eigenvalues (characteristic multipliers) of the Jacobian derived in the foregoing. In particular, we are interested in the variation of the eigenvalues as some chosen parameters are varied. This information essentially reveals the bifurcation phenomena and the way in which the variation of parameters affects the operation of the system.

By solving the cubic equation (11), five characteristic multipliers λ_1, λ_2, λ_3, λ_4, and λ_5 are obtained by expansion and contraction near the operating point, and therefore they can characterize its stability. When all the characteristic multipliers are in the left half plane of the complex plane, the system is stable. In particular, when a couple of complex conjugate characteristic multipliers simultaneously stay on the imaginary axis, a Hopf bifurcation occurs.[15,17–19] The characteris-

tic multipliers for different values of K_{ii} at $K_{pi} = 6$, $I_{max} = 5$ A are given in Table 3, showing that a Hopf bifurcation takes place at $K_{ii} = 7.266$. The characteristic multipliers for different values of K_{pi} at $K_{ii} = 8.551$, $I_{max} = 5$ A are given in Table 4, showing that a Hopf bifurcation takes place at $K_{pi} = 8.000$. The locus is plotted in Fig. 9 for ease of reference.

Table 3. Characteristic multipliers for different values of K_{ii} at $K_{pi} = 6$, $I_{max} = 5$.

K_{ii}	$\lambda_1/10^{-3}$	$\lambda_2/10^{-3}$	$\lambda_3/10^{-3}$	$\lambda_4/10^{-3}$	$\lambda_5/10^{-3}$	Remark
1.00	–0.0152 + 1.2750i	–0.0152–1.2750i	–0.0617 + 0.1017i	–0.0617–0.1017i	–0.0079	stable
3.00	–0.0095 + 1.3266i	–0.0095–1.3266i	–0.0673 + 0.1862i	–0.0673–0.1862i	–0.0080	stable
5.00	–0.0047 + 1.3777i	–0.0047–1.3777i	–0.0722 + 0.2353i	–0.0722–0.2353i	–0.0081	stable
7.00	–0.0006 + 1.4280i	–0.0006–1.4280i	–0.0763 + 0.2704i	–0.0763–0.2704i	–0.0081	stable
7.26	–0.0000 + 1.4346i	–0.0000–1.4346i	–0.0768 + 0.2744i	–0.0768–0.2744i	–0.0081	Hopf bifurcation
8.00	0.0013 + 1.4528i	-0.0013–1.4528i	–0.0781 + 0.2847i	–0.0781–0.2847i	–0.0082	unstable
9.00	0.0030 + 1.4773i	-0.0030–1.4773i	–0.0799 + 0.2974i	–0.0799–0.2974i	–0.0082	unstable
10.0	0.0046 + 1.5016i	-0.0046–1.5016i	–0.0815 + 0.3088i	–0.0815–0.3088i	–0.0082	unstable

Table 4. Characteristic multipliers for different values of K_{pi} at $K_{ii} = 8.551$, $I_{max} = 5$.

K_{pi}	$\lambda_1/10^{-3}$	$\lambda_2/10^{-3}$	$\lambda_3/10^{-3}$	$\lambda_4/10^{-3}$	$\lambda_5/10^{-3}$	Remark
1.00	0.0079 + 1.4659i	0.0079–1.4659i	–0.0786 + 0.2921i	–0.0786 - 0.2921i	–0.0080	unstable
3.00	0.0056 + 1.4661i	0.0056–1.4661i	–0.0788 + 0.2920i	–0.0788 - 0.2920i	–0.0080	unstable
5.00	0.0034 + 1.4662i	0.0034–1.4662i	–0.0790 + 0.2919i	–0.0790 - 0.2919i	–0.0081	unstable
7.00	0.0011 + 1.4664i	0.0011–1.4664i	–0.0792 + 0.2918i	–0.0792 - 0.2918i	–0.0081	unstable
8.00	–0.0000 + 1.4665i	–0.0000–1.4665i	–0.0793 + 0.2918i	–0.0793 - 0.2918i	–0.0081	Hopf bifurcation
9.00	–0.0011 + 1.4665i	–0.0011–1.4665i	–0.0794 + 0.2917i	–0.0794 - 0.2917i	–0.0081	stable
10.0	–0.0023 + 1.4666i	–0.0023–1.4666i	–0.0795 + 0.2917i	–0.0795 - 0.2917i	–0.0082	stable
11.0	–0.0034 + 1.4667i	–0.0034–1.4667i	–0.0797 + 0.2917i	–0.0797 - 0.2917i	–0.0082	stable

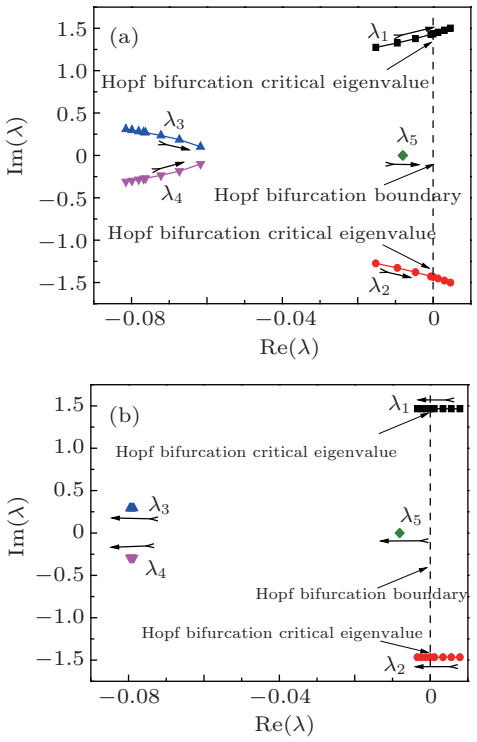


Fig. 9. (color online) Loci of the complex eigenvalue pair corresponding to Tables 3 and 4, showing (a) the characteristic multipliers for K_{ii} from 1 to 10, and (b) the characteristic multipliers for K_{pi} from 1 to 10.

According to the homotopy function theory,[20–22] λ_1 and λ_2 correspond to i_L and i_a, respectively. From the analysis above, it can be found that only λ_1 and λ_2 move across the imaginary axis no matter which bifurcation parameter is chosen, while the other characteristic multipliers stay in the left half plane all the time. In other words, the current of the inductor loses stability first regardless of the choice of bifurcation parameters when the Hopf bifurcation occurs. For the average current controlled FESS, the duty ratio signal is generated according to the measured current of the inductor. Therefore, the primary cause of the bifurcation behavior is the loss of control over the inductor current. The slow oscillation of the duty ratio in the Hopf bifurcation state is shown clearly in Fig. 10. In this sense, the duty ratio D reflects the essential characteristics of the dynamics of the FESS.

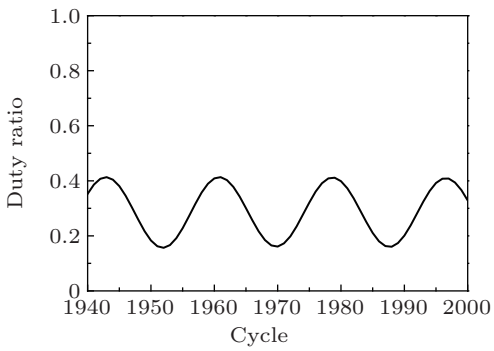


Fig. 10. Duty ratio in the Hopf bifurcation state.

3.2.3. Stability region estimation

To be ready for practical applications, some behavior boundaries should be given in the parameter space. Such boundaries can provide plenty of design-oriented information, which allows the system parameters to be selected in an informed manner for obtaining a stable operation system. Using these boundaries, engineers can not only identify the type of Hopf bifurcation, but also know how to place the nominal operating point away from the behavior boundaries.

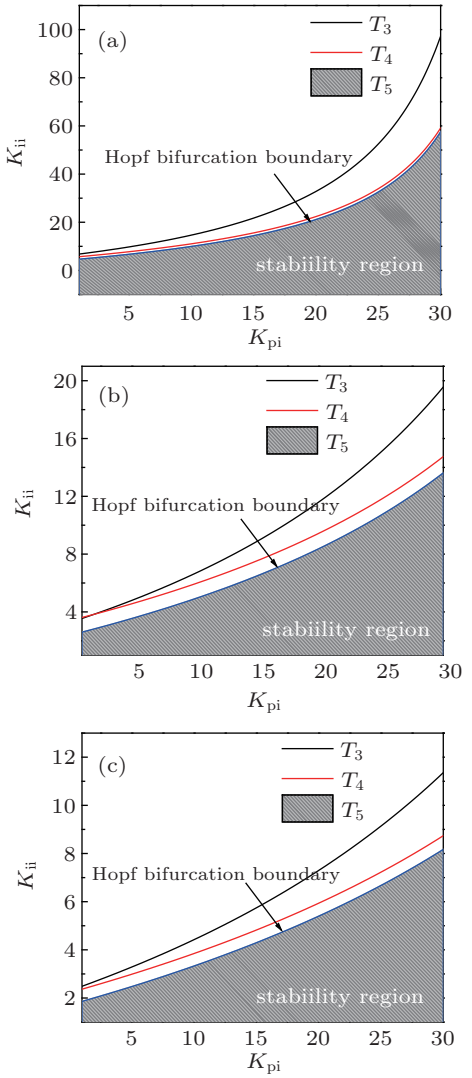


Fig. 11. Stability region in the (K_{pi}, K_{ii}) plane when (a) $I_{max} = 5$ A, (b) $I_{max} = 10$ A, (c) $I_{max} = 15$ A.

According to Table 2 and taking $I_{max} = 5$, 10, 15 for example, considering the real parameter values of the FESS in Table 1, we find that $T_1 = a_0 = 1 > 0$ and $T_2 = a_1 = (B_v CL_m + CJR_m + CJL_m s_1)/(CJL_m) > 0$ can be always satisfied, then only the positive regions of T_3, T_4, T_5, and T_6 are to be considered. Figure 11 shows the curves of $T_3 = 0$, $T_4 = 0$, and $T_5 = 0$. The regions below the three curves are the positive regions (for the parameters of the FESS used in this paper, close to the computed results, $T_6 > 0$ is always satisfied). By taking the intersection, the stability region is located in the area under the critical curve $T_5 = 0$, which is shaded in gray (Fig. 11).

Strictly speaking, Eq. (14) does not give a formal condition for the occurrence of Hopf bifurcation. By considering the previous studies for the Hopf–Routh bifurcation criterion.[23,24] and combining with Table 2, the exact Hopf bifurcation boundary conditions can be expressed as

$$\begin{aligned} &T_5 = 0, \\ &T_i > 0, \quad (i = 1,2,3,4)\,. \end{aligned} \tag{15}$$

By considering the analytical result obtained from the critical curves in the (K_{pi}, K_{ii}) plane in Fig. 11, the $T_5 = 0$ critical curve can be taken as the Hopf bifurcation boundary condition

$$\begin{aligned} \delta(5, K_{pi}) &= 5.29651 - 0.24676K_{pi} + 0.12954K_{pi}^2 \\ &\quad - 0.00744K_{pi}^3 + 1.7621 \times 10^{-4} K_{pi}^4, \\ \delta(10, K_{pi}) &= 2.38978 + 0.21137K_{pi} + 0.00403K_{pi}^2 \\ &\quad - 4.02744 \times 10^{-5} K_{pi}^3 + 2.90335 \times 10^{-6} K_{pi}^4, \\ \delta(15, K_{pi}) &= 1.715 + 0.14339K_{pi} + 0.00173K_{pi}^2 + 2.50926 \\ &\quad \times 10^{-6} K_{pi}^3 + 6.52305 \times 10^{-7} K_{pi}^4. \end{aligned} \tag{16}$$

The typical critical values of the control parameters can be calculated from the critical curves above, as shown in Table 5.

An interesting phenomenon appears during the operation of a real FESS, the limit cycle oscillation occurs before the parameters of the control system enter into the instability region, which is due to the quantization effect. An unexpected oscillation appears even at values of K_{pi} and K_{ii} which satisfy the stability conditions established by the Routh analysis.

Despite the resolutions satisfying the static no-limit-cycle conditions, limit cycles can come forth because of the dynamic gain caused by the quantizer.[25] By taking the worst case into account, AD and DPWM would both have maximum equivalent gain $4/\pi$. The stability region (14) can be rewritten as follows:

$$0 < K_{ii} < \left(\frac{\pi}{4}\right)^2 \delta\left(I_{max}, \left(\frac{4}{\pi}\right)^2 K_{pi}\right). \tag{17}$$

Using Eq. (17), the new boundary of the stability region can be located again, as shown in Fig. 12.

Table 5. Typical critical values of control parameters.

$I_{max} = 5$ A										
K_{pi}	1.00	2.00	3.00	4.00	5.00	6.00	7.00	8.00	9.00	10.00
K_{ii}	4.67	5.15	5.67	6.19	6.76	7.26	7.89	8.55	9.24	9.98
K_{pi}	11.0	12.00	13.00	14.00	15.00	16.00	17.00	18.00	19.00	20.00
K_{ii}	10.7	11.63	12.54	13.38	14.43	15.56	16.80	18.16	19.64	21.28
$I_{max} = 10$ A										
K_{pi}	1.00	2.00	3.00	4.00	5.00	6.00	7.00	8.00	9.00	10.00
K_{ii}	2.60	2.83	3.07	3.31	3.56	3.78	4.05	4.33	4.61	4.90
K_{pi}	11.0	12.00	13.00	14.00	15.00	16.00	17.00	18.00	19.00	20.00
K_{ii}	5.20	5.51	5.79	6.12	6.47	6.82	7.20	7.59	7.98	8.34
$I_{max} = 15$ A										
K_{pi}	1.00	2.00	3.00	4.00	5.00	6.00	7.00	8.00	9.00	10.00
K_{ii}	1.85	2.01	2.16	2.32	2.48	2.63	2.80	2.97	3.15	3.33
K_{pi}	11.0	12.00	13.00	14.00	15.00	16.00	17.00	18.00	19.00	20.00
K_{ii}	3.52	3.71	3.88	4.08	4.29	4.50	4.72	4.95	5.11	5.38

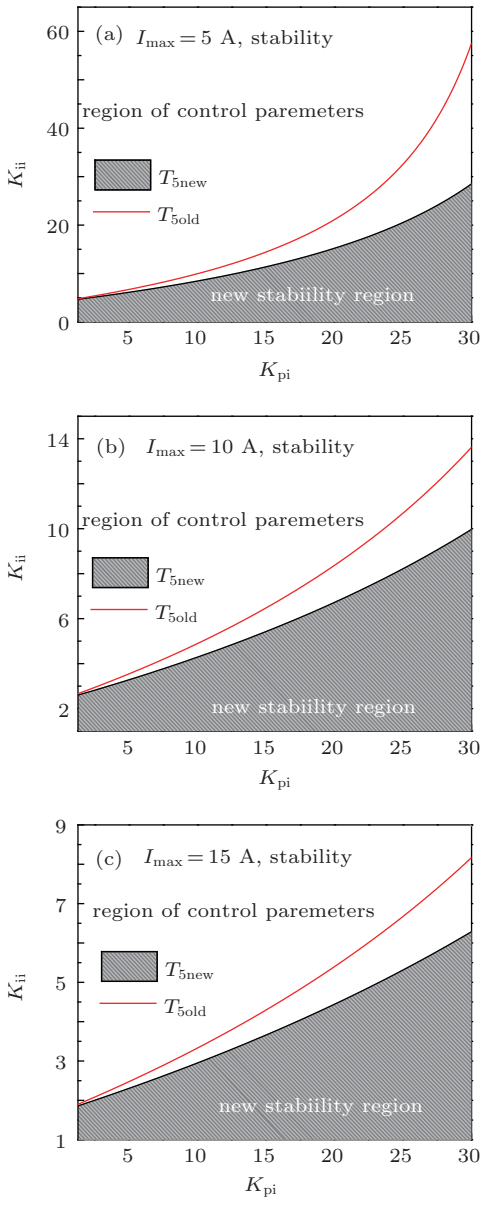


Fig. 12. (color online) Estimated stability region in (K_{pi},K_{ii}) plane by considering the quantization effect of the digital control system when (a) $I_{max} = 5$ A, (b) $I_{max} = 10$ A, (c) $I_{max} = 15$ A.

4. Experimental verification

To verify the above theoretical analysis, experiments are carried out on an FESS platform, which is shown in Fig. 13.[26,27] The parameters are set to those in Table 1. The IGBT module is IRG4PH50UD from the IR Company, the drive chip is M57962AL from the Mitsubishi Electric Company, and the IPM is PS21267 from the Mitsubishi Electric Company. The voltage signals are transformed by Hall sensors. The transformation ratio of the oscilloscope probe is 10 : 1. Under such conditions, the result is 1 V for 4 A and 1 V for 40 V. As a result, the vibration of the voltage seems smaller than that of the current. The waveforms of current and voltage shown in Figs. 14–17 match the phenomenon observed from the simulations well.

Based on the system parameters and the control parameters, the corresponding switching frequency is selected as 4 kHz, the effect of switching noise on the system dynamics can be ignored. Set $I_{max} = 5$ A and $K_{pi} = 6$, the integral gain K_{ii} is first given a small value. The FESS operates at the steady period-1 state when the integral gain is $K_{ii} = 1$, as shown in Fig. 14, the waveform of i_L is a steady triangular wave and v is a constant over time. At $K_{ii} = 7.2$, a nearly sinusoidal limit cycle and quasi-periodic oscillation behavior appears, as K_{ii} increases up to the critical value of the Hopf bifurcation, as shown in Fig. 15, the waveform of i_L mixes with a sinusoidal oscillation of a small amplitude and little has been changed for v, which confirms the foregoing analysis. Therefore, the control parameters tested with the analog controlled converter cannot be converted into the digitally controlled ones directly because of the phase delay brought by the ZOH and the quantization effect induced by the DPWM. The limit cycle due to the quantization effect and the slow scale low frequency oscil-

lation in the FESS are not desirable and therefore should be avoided. Then set $K_{ii} = 7.3$, it can be observed that the Hopf bifurcation oscillation takes place and a limit cycle appears, as shown in Fig. 16. The trajectories of i_L and v lose stability and a Hopf bifurcation oscillation with stable frequency and amplitude apears, and the peak-to-peak current oscillation amplitude can be as high as 8 A. In Fig. 17, a chaotic behavior of the phase current in the BLDCM is observed for $K_{ii} = 7.3$, an evident oscillation exists in this phase current. Here the influence of the power electronic subsystem on the motor running state can be clearly noticed.

Comparing the results of simulation, platform experiments, and theoretical analysis, deviations can still be observed. The main reasons are as follows. 1) The system description of the FESS is approximate. 2) Errors between the measured and actual values of the system parameters cannot be completely avoided. 3) The parasitic parameters of the FESS have not been considered.



Fig. 13. (color online) A real FESS in the lab.

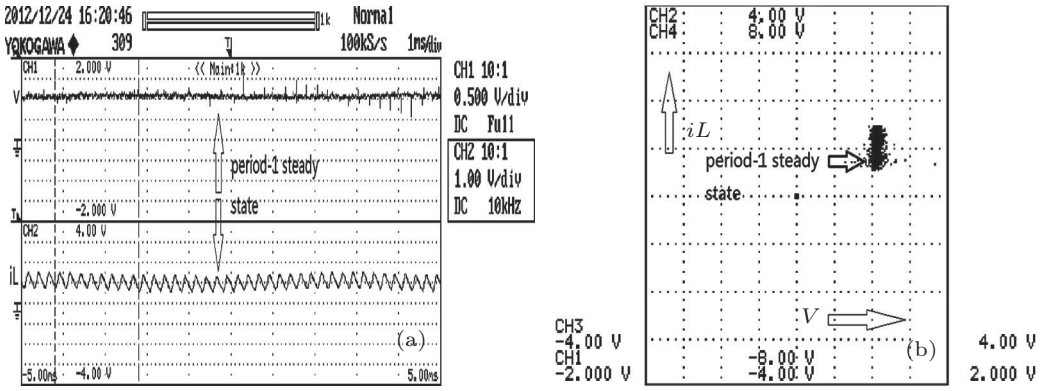


Fig. 14. Period-1 steady state behavior of the FESS platform when $I_{max} = 5$ A, $K_{pi} = 6$, $K_{ii} = 1$: (a) the measured waveforms of i_L and v, (b) phase trajectory of the platform with i_L and v.

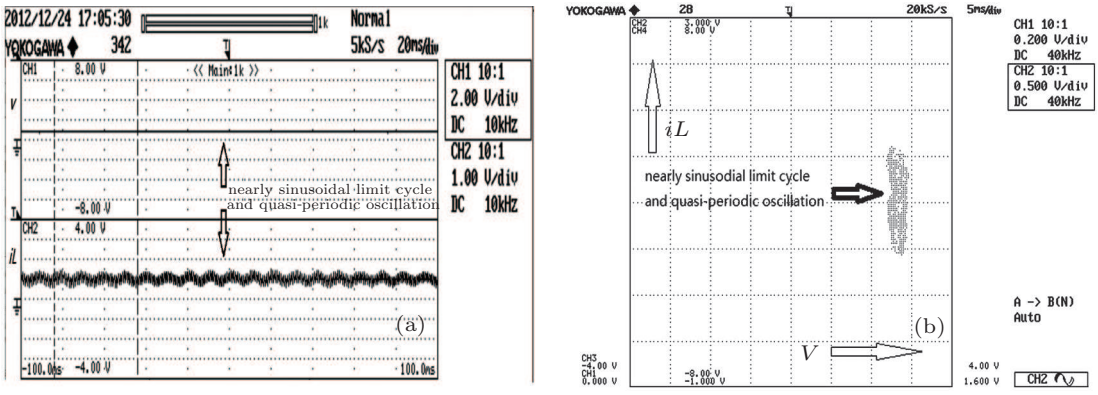


Fig. 15. Nearly sinusoidal limit cycle and quasi-periodic oscillation behavior of the FESS platform when $I_{max} = 5$ A, $K_{pi} = 6$, $K_{ii} = 7.2$: (a) measured waveforms of i_L and v, (b) phase trajectory of the platform with i_L and v.

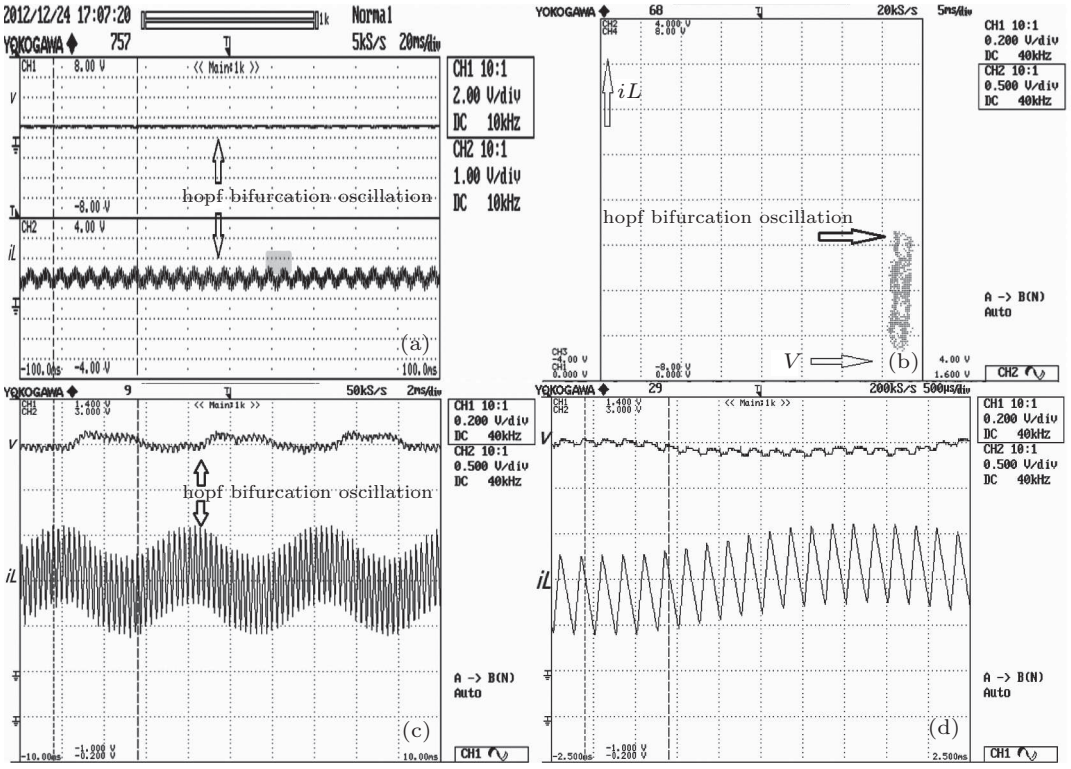


Fig. 16. Hopf bifurcation oscillation behavior of the FESS platform when $I_{\max} = 5$ A, $K_{\rm pi} = 6$, $K_{\rm ii} = 7.3$: (a) measured waveforms of i_L and v, (b) phase trajectory of the platform with i_L and v, (c) close-up view of (a), (d) close-up view of (c).

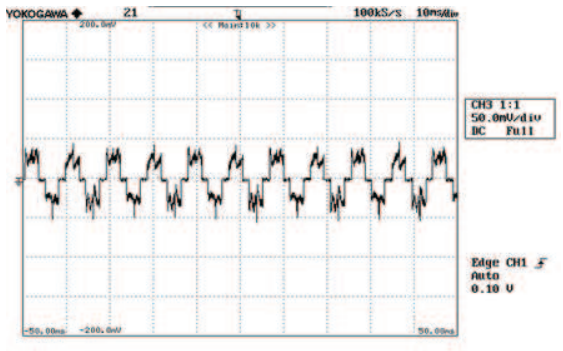


Fig. 17. Phase current of the BLDCM in Fig. 16.

5. Conclusion

The FESS has become a primary choice for energy storage due to its high efficiency and low cost, and is now widely used in power systems. This paper deals with the generation process and mechanism of the coupled dynamic behavior of the FESS, especially the interaction between power electronic subsystem and mechanical subsystem. Extensive analysis and discussion of the Hopf bifurcation and chaotic behavior in an average current controlled FESS have been carried out. Research in this paper shows that the Hopf bifurcation in the electric transmission process of the FESS is directly due to the loss of control over the inductor current, which is caused by the system control parameters exceeding certain ranges. When such an instability occurs, the system inevitably enters into a complex transition state of the coexistence of fast-scale and slow-scale behaviors. Conclusions can be drawn that for an electromechanical coupling system like an FESS, a larger proportional coefficient leads to a more stable state; meanwhile, a larger integral coefficient reduces the stability. Through determining and modifying the parameter stability regions with the Hopf–Routh bifurcation criterion, the instability problems can be eliminated considering the effects of the quantization error. This provides a certain guide for the design and control of an FESS in power systems. Finally, an experimental FESS prototype is built to verify the analyses and research results in this paper. The approach adopted in the paper is clear logically and well-defined physically, which makes it useful for forecasting and discovering the chaotic behaviors in an FESS or other similar systems. The work is of great significance for improving the stability and reliability of the FESS and of benefit to the development of renewable resources.

References

[1] Park J D, Kalev C and Holfmann H F 2008 *IEEE Transactions on Industrial Electronics* **55** 3038

[2] Zhang Y K and Jiang S Y 2004 *Acta Energiae Solaris Sinica* **25** 254 (in Chinese)

[3] Hemati N 1994 *IEEE Transactions on Circuits and Systems I: Fundamental Theory and Applications* **41** 40

[4] Jiang S Y and Ju L H 2006 *Science in China Serises E* **49** 61

[5] Coombs T A, Campbell A M, Ganney I, Lo W, Twardowski T and Dawson B 1998 *Materials Science and Engineering B Solid State Materials for Advanced Technology* **53** 225
[6] Chen W J 1996 *Journal of Engineering for Gas Turbine and Power* **118** 115
[7] Yu Y and Mi Z Q 2013 *Acta Phys. Sin.* **62** 0384031 (in Chinese)
[8] Li C L, Yu S M and Luo X S 2012 *Chin. Phys. B* **21** 100506
[9] Li Z, Jin B P, Young H J, Zhang B and Chen G 2002 *IEEE Transactions on Circuits and Systems I: Fundamental Theory and Applications* **49** 383
[10] Dai D, Ma X K, Zhang B and Tse C K 2009 *Chaos Soliton. Fract.* **41** 1027
[11] Mazumder S K, Nayfeh A H and Boroyevich D 2001 *IEEE Transcations on Power Electronics* **16** 201
[12] Xia C L, Song P, Shi T N and Yan Y 2011 *IEEE Transactions on Industrial Electronics* **60** 78
[13] Iu H H C and Tse C K 2003 *IEEE Transactions on Circuits and Systems I: Fundamental Theory and Applications* **50** 679
[14] Ren H P and Liu D 2005 *Chin. Phys. B* **14** 1352
[15] Zhao Y B, Zhang D Y and Zhang C J 2007 *Chin. Phys.* **16** 933
[16] Zhou G H, Bao B C, Xu J P and Jin Y Y 2010 *Chin. Phys. B* **19** 050509
[17] Wei D Q and Zhang B 2009 *Chin. Phys. B* **18** 1399
[18] Yang N N, Liu C X and Wu C J 2012 *Chin. Phys. B* **21** 080503
[19] Tse C K, Lai Y M and Iu H H C 2000 *IEEE Transactions on Circuits and Systems I: Fundamental Theory and Applications* **47** 448
[20] Melville R C, Trajkovic L, Fang S C and Watson L T 1993 *IEEE Transactions on Computer-Aided Design of Integrated Circuits and Systems* **12** 861
[21] Bergner J E 2007 *Topology* **46** 397
[22] Zhao J Q and Zhang B M 2005 *Automation of Electric Power Systems* **29** 91
[23] Wang F Q, Ma X K and Yan Y 2011 *Acta Phys. Sin.* **60** 0605101 (in Chinese)
[24] Dai D, Tse C K, Zhang B and Ma X 2008 *International Journal of Bifurcation and Chaos* **18** 2095
[25] El Aroudi A, Benadero L, Toribio E and Olivar G 1999 *IEEE Transactions on Circuits and Systems I: Fundamental Theory and Applications* **46** 1374
[26] Yuan J Q 2012 High power DC/DC Converter for Flywheel Energy Storage System (MS Thesis) (Tianjin: Tianjin University) (in Chinese)
[27] Tan Z and Li Y L 2012 *Power System Protection and Control* **40** 127 (in Chinese)